



HAL
open science

Sliding droplets in a laminar or turbulent boundary layer

Antonio Chahine, Julien Sebilleau, Romain Mathis, Dominique Legendre

► **To cite this version:**

Antonio Chahine, Julien Sebilleau, Romain Mathis, Dominique Legendre. Sliding droplets in a laminar or turbulent boundary layer. *Physical Review Fluids*, 2022, 7 (11), pp.113605. 10.1103/PhysRevFluids.7.113605 . hal-04072500

HAL Id: hal-04072500

<https://hal.science/hal-04072500v1>

Submitted on 18 Apr 2023

HAL is a multi-disciplinary open access archive for the deposit and dissemination of scientific research documents, whether they are published or not. The documents may come from teaching and research institutions in France or abroad, or from public or private research centers.

L'archive ouverte pluridisciplinaire **HAL**, est destinée au dépôt et à la diffusion de documents scientifiques de niveau recherche, publiés ou non, émanant des établissements d'enseignement et de recherche français ou étrangers, des laboratoires publics ou privés.

Sliding droplets in a laminar or turbulent boundary layer

A. Chahine, J. Sebilleau, R. Mathis, and D. Legendre

Institut de Mécanique des Fluides de Toulouse (IMFT),

Institut National Polytechnique de Toulouse,

2 Allée du Professeur Camille Soula, 31400 Toulouse, France

Abstract

In this study, we report an experimental investigation of droplet sliding under the influence of a laminar or turbulent airflow for water and glycerin droplets. The onset of sliding is described thanks to a critical Weber number, based on the mean airflow velocity impacting the droplet, depending upon the contact angle hysteresis and a drag coefficient (that also depends on the Reynolds number). A fairly good agreement is observed with our experiments and various data from the literature. The transitions between the various droplet shapes observed during sliding (oval, corner, and rivulet) are characterized in a phase diagram built on the droplet capillary and Bond numbers.

Keywords: Droplet, Shear flow, Boundary layer, Critical velocity

I. INTRODUCTION

Sliding droplets on a solid surface is a common phenomenon that can be observed on windows and windshields during rainy days. This situation, that occurs when an external force (such as gravity and aerodynamic forces) overcomes the capillary force, is of fundamental interest because of the subtle hydrodynamics near the contact line. The case of droplets sliding along an inclined wall under partial wetting conditions has been studied since the 1950's [1–7]. In this situation, the onset of sliding is predicted thanks to a balance between gravity and capillary forces leading to critical Bond number that depends on the substrate inclination and the contact angle hysteresis: $Bo_c = \rho_d g \sin(\alpha) V_d^{2/3} / \sigma \propto \cos \theta_r - \cos \theta_a$ where ρ_d , V_d and σ are respectively the droplet density, volume and surface tension, α is the inclination of the substrate and θ_r and θ_a are the receding and advancing contact angles. Then depending on its velocity, the droplet can adopt three different shapes: oval, corner, or cusp shape.

The case of droplets sliding on an horizontal substrate under the effect of an airflow has also received some attention in the past decades [8–20]. Experiments have been performed for laminar [10, 12, 14, 16, 18–20] or turbulent [13, 15, 16] boundary layer while theoretical and numerical studies have addressed the case of a linear shear flow [8, 9]. In these studies, the onset of sliding is generally predicted thanks to a balance between the drag force and the capillary force leading to a critical Weber number that depends on the contact angle hysteresis. Then, depending on its velocity, the droplet can adopt four different shapes: oval, corner, cusp, and rivulet shape. The latter is characterized by a long tail [17] that does not appear for droplets sliding on an inclined wall. The onset on sliding under the effect of an external airflow is usually reported using a critical Weber number $We = \rho_a U_c^2 H / \sigma$, where ρ_a is the air density, H is the height of the droplet and U_c is a characteristic velocity either defined as the gas velocity U_∞ far from the substrate [12, 16–18, 21] or constructed using the shear rate $\frac{\partial U}{\partial z}$ [8, 9, 14, 18]. The resulting values of We and operating conditions are reported in Table I. It results in critical Weber numbers that differ about one order of magnitude for similar wetting conditions as illustrated in Fig. 1 where only measurements for water droplets are presented. It is also noticeable that, in these experiments, the droplets height and its ratio with boundary layer thickness δ estimated here with the scaling of Blasius theory for laminar boundary layer ($\delta = \sqrt{\frac{\nu_a x}{U_\infty}}$, where ν_a is the air viscosity and x the distance

to the leading edge) can change significantly as shown in Table I. Thus, some experiments are performed for droplets inside the linear part of the boundary layer ($\frac{H}{\delta} < 5$) while in the rest the gas flow is no longer a linear sheared flow ($\frac{H}{\delta} > 5$).

TABLE I: Critical depinning conditions for water droplets reported in literature We and calculated We_c ; θ_m is the mean contact angle at depining; studies marked with \star are experiments conducted in turbulent channel flows, and otherwise in laminar boundary layers formed over flat plates.

	Substrate	V_d (μL)	U_c (m/s)	θ_m (deg)	H (mm)	H/δ	We	We_c	
Weber number We constructed using the shear rate									
Roisman <i>et al.</i> [14] (■)	PDMS	50	3.8	79	2.6	7.316	0.6	0.630	
		100	3.5	79	3.3	8.846	0.7	1.259	
	PMMA	50	3.2	80	2.6	6.779	0.4	0.460	
		100	3.2	80	3.3	8.541	0.6	0.574	
	Teflon	50	2.6	113	3.5	8.034	0.3	0.441	
		100	2.5	113	4.4	9.926	0.4	0.813	
	SHS	50	2.2	150	4.3	9.160	0.3	0.612	
		100	2.2	150	5.4	11.541	0.4	1.224	
	Zhang [20] (▽)	PMMA	75	17.8	82	2.5	2.660	6.9	1.926
			90	17.2	81.2	2.6	2.766	7.0	2.001
105			18.2	83	2.7	2.872	8.3	2.425	
120			16.8	83.5	2.8	2.979	7.7	2.309	
Seiler <i>et al.</i> \star [15] (◀)	Aluminum	35	3.4	63	2.0	7.242	1.7	-	
	Aluminum (varnished)	35	3.3	60	1.9	6.885	1.6	-	
	PMMA	35	3.2	59	1.9	6.698	1.5	-	
	Steel (varnished)	35	3.5	50	1.7	6.223	1.8	-	
	Weber number We constructed using the gas velocity								
Milne and Amirfazli [10] (●)	PMMA	58	4.8	66	2.2	8.388	1.8	0.860	
		100	3.5	66	2.4	7.814	1.6	0.500	
Hooshanginejad and Lee [22] (◇)	Aluminum (rough)	130	20.8	49	2.0	4.933	8.5	0.674	
White and Schmucker [19] (▲)	Aluminum (rough)	75	14.8	51	2.1	4.481	7.6	0.301	
		100	14.5	51	2.5	5.281	7.8	0.481	
		150	13.5	51	2.8	5.707	7.6	0.539	
Barwari <i>et al.</i> \star [16] (▶)	PMMA	39.9	10	51	1.8	10.356	3.6	-	
	Silicon (coated)	39.9	5.2	90	2.7	11.944	1.3	-	

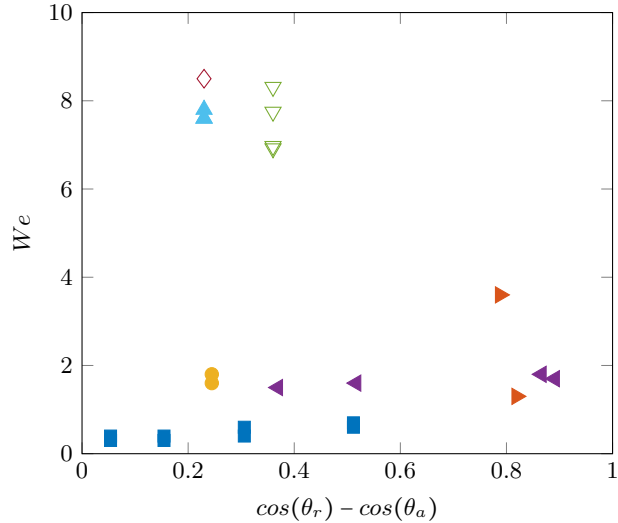


FIG. 1: Critical Weber number We as a function of the hysteresis at the contact line $\cos(\theta_r) - \cos(\theta_a)$ as reported in literature for water droplet. The symbols represent different droplet sizes with respect to the boundary layer: open symbols for $H/\delta < 5$ and solid symbols for $H/\delta > 5$. (●), Milne and Amirfazli [10]; (■), Roisman *et al.* [14]; (◄), Seiler *et al.* [15]; (▶), Barwari *et al.* [16]; (◇), Hooshanginejad and Lee [22]; (▲), White and Schmucker [19]; (▽), Zhang [23].

The aim of the present work is to clarify the onset of sliding prediction and to characterize the different shapes adopted by the sliding droplet thanks to two synchronized views (from the side and the bottom) with two different liquids (water and glycerin). In the following, we first introduce the experimental apparatus and the procedures employed for these measurements (Sec. II), then we present our experimental results obtained and compare them with the theory (Sec. III) and finally concludes this work (Sec. IV).

II. EXPERIMENTAL CONFIGURATION

The experiments were performed inside a closed-loop wind tunnel depicted in Fig. 2 (a). This facility has a working test section of $0.8 \text{ m} \times 0.5 \text{ m} \times 2.0 \text{ m}$ with a maximum free-stream velocity of 30 m/s and a free-stream turbulence intensity less than 0.1% . A 1.2 m long aluminum plate with a 3D print leading edge (to ensure a laminar boundary layer) is placed at the mid-height of the test section. This plate was designed to host a glass plate of $200 \text{ mm} \times 100 \text{ mm}$ at a distance of 600 mm from the leading edge (see Fig. 2 (a), (b),

and (c)), where the droplets are deposited with a micro-pipette. Prior to experiments, the glass plate was treated with a commercial rainproof product named *Rain-X*. This product consists of a hydrophobic silicone polymer that renders the glass hydrophobic (with typical contact angles about 90°). According to the manufacturer’s recommendation, the treatment was applied as follows:

1. the surface is cleaned with water,
2. the *Rain-X* is applied on the glass by rubbing in a circular motion a cloth,
3. the substrate is allowed to dry. Any excess powder on the glass is cleaned until a fully transparent surface is achieved.

The wetting conditions were tested by measuring the advancing and receding contact angles on several locations of the treated glass substrate thanks to a KRUSS, EASYDROP goniometer. The mean advancing and receding contact angles ($\theta_{a,s} - \theta_{a,r}$) were observed to be quite homogeneous on the treated glass surface with values ($87^\circ - 83^\circ$) and ($92^\circ - 86^\circ$) for water and glycerol droplets, respectively. The droplet deformation and sliding were recorded by shadowgraphy using two Imager SCMOS cameras from Lavision (see Fig. 2 (d)), with a resolution of $2560 \text{ pix} \times 2160 \text{ pix}$, at a frame rate of 100 fps. The side view field is approximately equal to $6.2 \text{ cm} \times 1.3 \text{ cm}$, and the bottom view is about $3.6 \text{ cm} \times 1.2 \text{ cm}$. Both cameras were synchronized to record at the same time. The recording begins when the wind tunnel is started. Each group of experiments was repeated at least two times under the same conditions. A summary of the experimental conditions is in Table III. The properties of the water and glycerol are presented in Table II.

TABLE II: Liquid properties: Dynamic viscosity μ , density ρ , surface tension σ and the test section temperature T .

Fluid	μ (Pa.s)	ρ (Kg/m ³)	σ (N/m)	T (°C)
Water	0.001	997	$75.64 * 10^{-3}$	20
Glycerol	1.1438	1260	$63.40 * 10^{-3}$	20

TABLE III: Experimental conditions: droplet volume V_d , surface wetting properties and inlet air flow velocity U_∞ and boundary layer (laminar vs turbulent).

Viscosity	V_d range (μL)	$\theta_{a,s}$ (deg)	$\theta_{r,s}$ (deg)	U_∞ range (m/s)	Laminar	Turbulent
Water	5-100	92 ± 2	75 ± 2	4-22	×	×
Glycerol	10-100	95 ± 2	80 ± 2	8-22	×	–

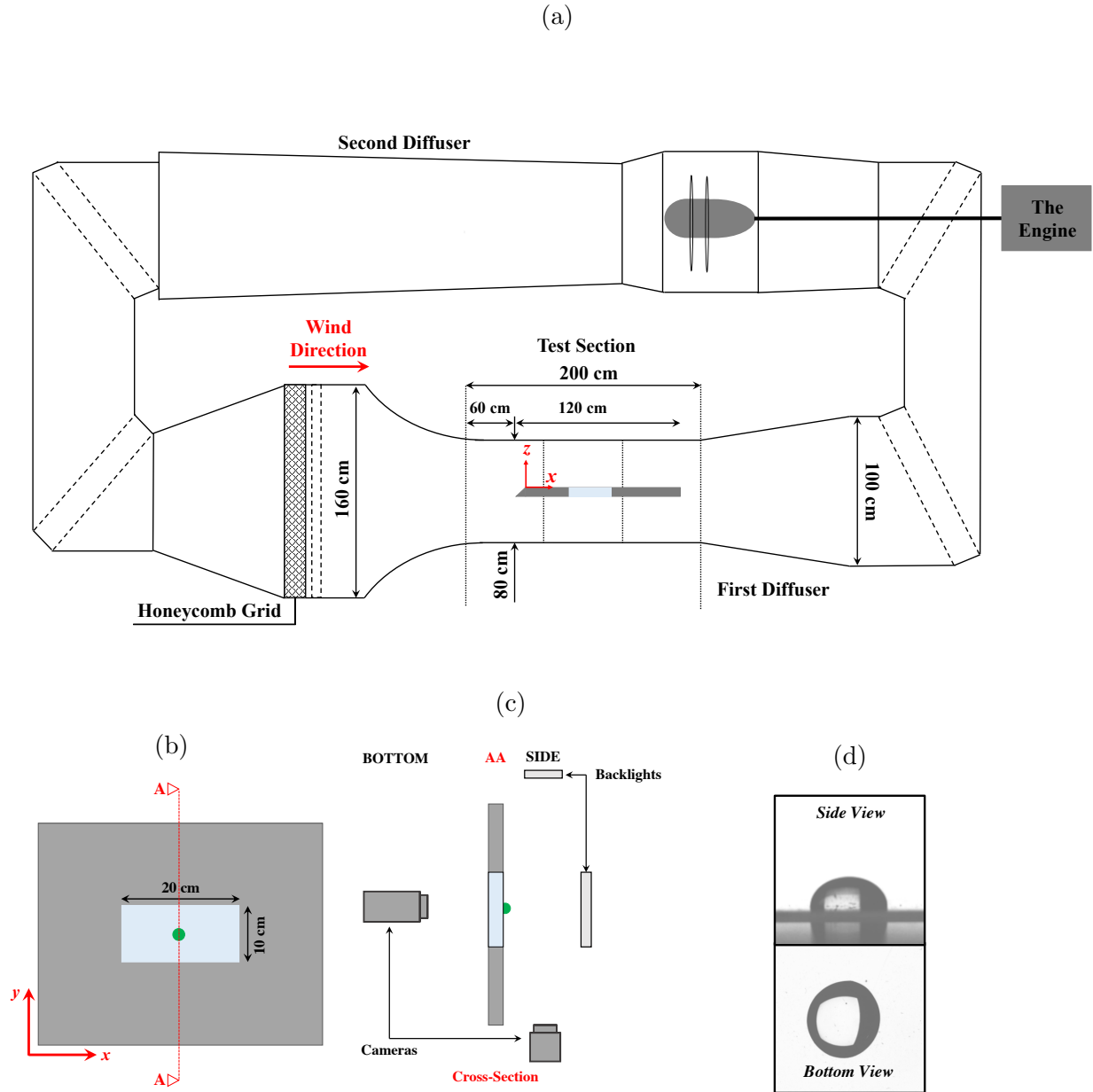


FIG. 2: Experimental Set-up: (a): The Wind Tunnel showing the bottom view setup. (b): Bottom View Set-up. (c): Side and Bottom View Set-up. (d): Examples of droplet photos taken by the cameras from side and bottom view.

The airflow over the glass plate (without droplets) was characterized with hot wire anemometry. Without any further modification of the leading edge, the flow profile corresponds to a laminar boundary layer and matches well with the Blasius boundary layer theory (see Fig. 3 (a)). To obtain a turbulent boundary layer, a sheet of sandpaper was

glued on the leading edge promoting turbulence. The flow profile in this case corresponds to a turbulent boundary layer fully-developed (see Fig. 3 (b)).

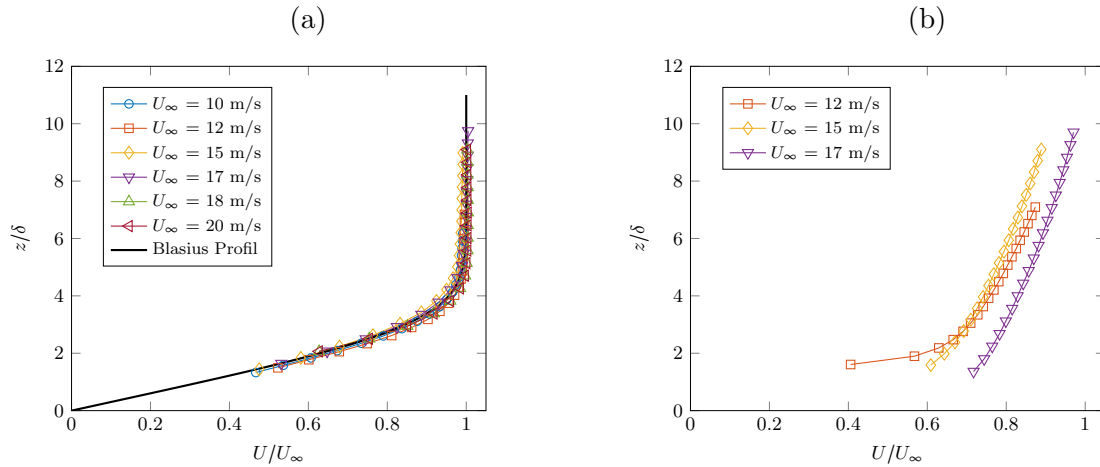


FIG. 3: Measurement of flow profiles for (a): Laminar Flow and (b): Turbulent Flow.

III. RESULTS

A. Shapes of sliding droplets

The use of two cameras allows to record simultaneous side and bottom views of the droplet during its motion. Typical experimental visualisations of glycerin and water droplets are presented in Fig. 4 and 5, respectively, for droplet volume $V_d = 40 \mu\text{L}$ and airflow with $U_\infty = 22$ m/s and $U_\infty = 20$ m/s respectively.

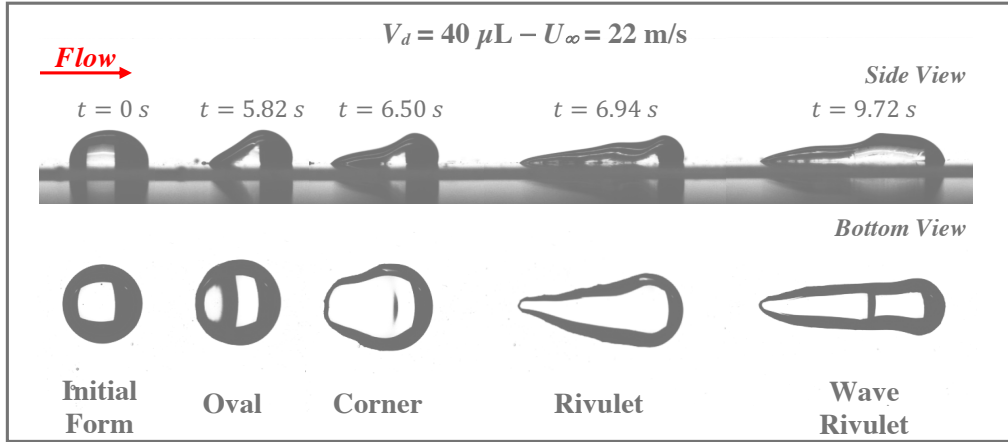


FIG. 4: Side and bottom views of a glycerol droplet submitted to a laminar shear flow on a glass surface, $V_d = 40 \mu\text{L} - U_\infty = 22 \text{ m/s}$.

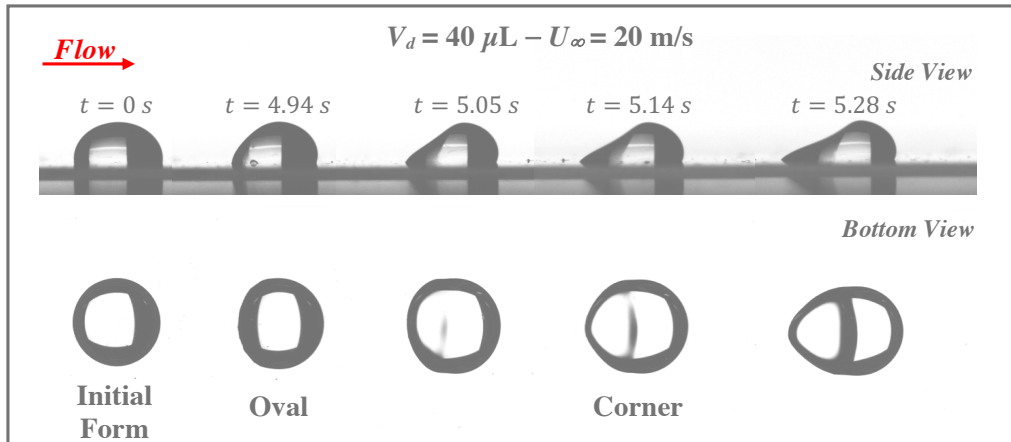


FIG. 5: Side and bottom views of a shedded water droplet submitted to a laminar shear flow on a glass surface, $V_d = 40 \mu\text{L} - U_\infty = 20 \text{ m/s}$.

As one can see, when submitted to a shear flow, the droplet initially axisymmetric deforms along the flow direction and can adopt various shapes during its sliding. For the glycerin droplet presented in Fig. 4, the initially axisymmetric droplet is firstly tilted in the airflow direction. Prior to the onset of sliding the downstream (receding) contact moves first leading to an oval shape that begins to move with the airflow. Then the shape evolves to a corner shape that can easily be recognized on the bottom view thanks to the formation of a wedge on the downstream contact line. This wedge eventually evolves toward a rivulet shape that

can exhibit waves on its surface if sufficiently long. These waves appear to have a strong influence on the droplet sliding but appear after the other sliding regimes (oval, corner and rivulet) and thus do not affect the onset of sliding. For water droplets, similar shapes are observed but additional oscillations can appear before the onset of sliding and remain for oval shapes. The appearance of these shapes depends on both the airflow conditions and the droplet volume. To further characterize these regimes, the latest droplet shapes observed (in the field of view of the cameras) are summarized for the studied volume and airflow conditions in Fig. 6 (a) and (b) for water droplets for laminar and turbulent boundary layer and in the Fig. 7 for glycerin droplets for laminar boundary layers. A similar trend is observed in the three figures. When moving along the diagonal with increasing both the droplets volume and the inlet flow velocity, the droplets shape varies from oval, to corner, then to rivulet. However, we can notice that immobile water droplets were observed at low velocity but not observed for glycerin droplets, a non-expected result because of droplets with a much larger fluid viscosity. The rivulet shape that only appears for sufficiently large droplets and velocities is not observed in laminar conditions for the range of water droplets considered here. The condition of sliding is discussed in the next section.

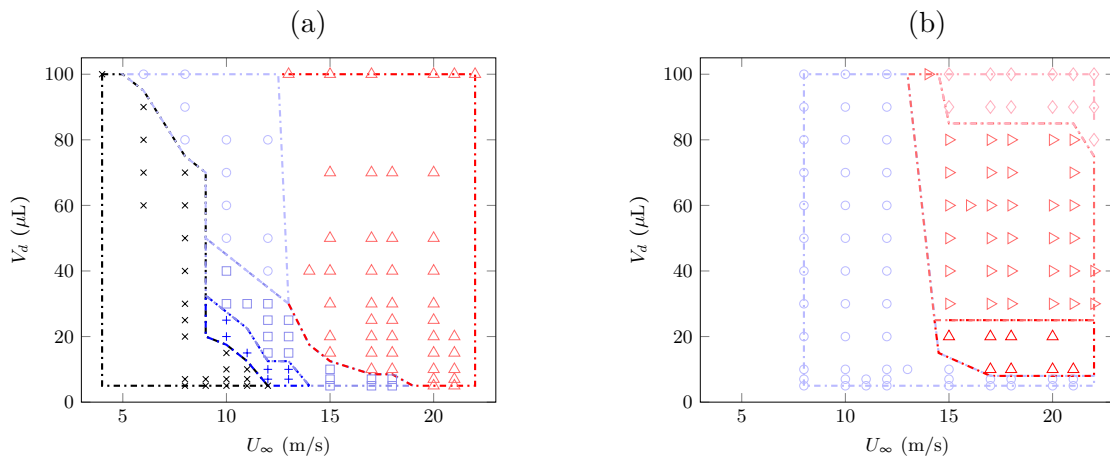


FIG. 6: Cartography of shape and behaviour for water droplets. (a): Laminar Flow. (b): Turbulent Flow. (\times), Oval Immobile; ($+$), Oval Oscillation & immobile; (\square), Oval Oscillation & moving; (\circ), Oval moving; (\triangle), Corner; (\triangleright), Rivulet; (\diamond), Long Rivulet.

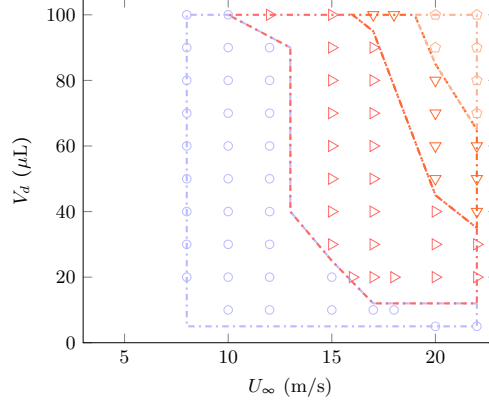


FIG. 7: Cartography of shape and behaviour for glycerol droplets (laminar flow only). (\circ), Oval moving; (\blacktriangleright), Rivulet; (\blacktriangledown), Rivulet Wave; (\circ), Rivulet Break-up.

B. Onset of sliding

The onset of sliding is defined by the simultaneous motion of the downstream (receding) and upstream (advancing contact line) of the droplet. This onset of sliding has been studied theoretically and numerically for droplets in a linear shear flow [8, 9]. Both these studies predict the onset of sliding through a critical shear rate that's scales with the contact angle hysteresis and the droplet volume as:

$$\left(\frac{\partial U}{\partial z}\right)_c \propto \frac{\sigma (\cos(\theta_r) - \cos(\theta_a))}{\mu_a V_d^{1/3}} \quad (1)$$

In our experiments with a laminar boundary layer, the droplet height is sufficiently small to have the entire droplet inside the linear sheared region of the boundary layer. Thus, using the velocity profile measurement depicted in Fig 3, the critical shear rate for this onset of sliding can be measured.

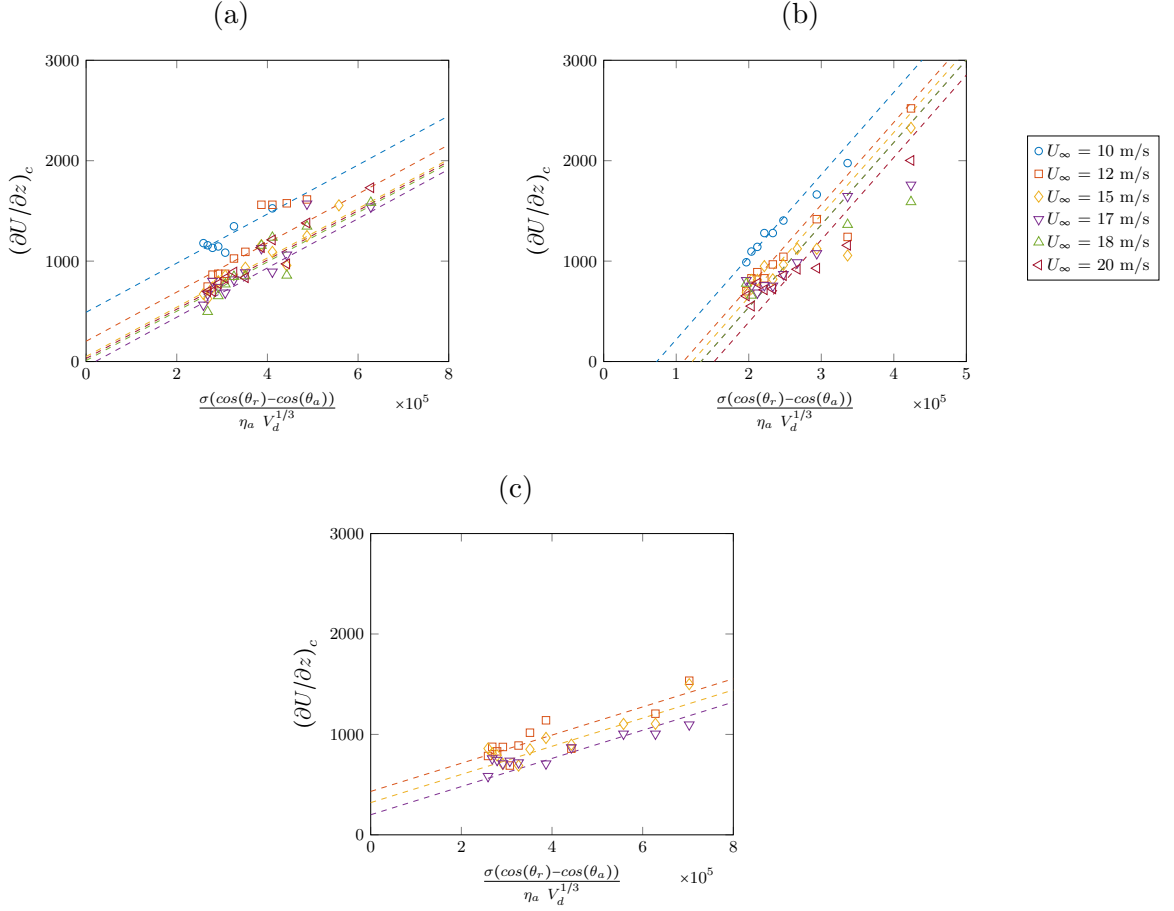


FIG. 8: Evolution of the critical shear rate $(\partial U/\partial z)_c$ as a function of Eq. (1): (a): water droplet in laminar flow. (b): glycerol droplet in laminar flow (c): water droplet in turbulent flow.

Fig. 8 (a) and (b) shows the evolution of the critical shear rate in a laminar boundary layer with the theoretical scaling law (Eq. 1) for a water and a glycerin droplets, respectively. As one can see, the measured critical shear rate appears to evolve linearly with this theoretical prediction. Nevertheless, the each airflow velocity U_∞ appears to have its own evolution meaning that the theoretical scaling law does not catch all the effects induced by the airflow when considering Eq. 1. Considering now our experiments in turbulent boundary layers, the droplet still remains inside the boundary layer but is no longer submitted to a linear shear. We thus propose to define an adapted shear rate with the ratio of the air velocity at the droplet height U_H determined using the turbulent boundary layer profile reported in Fig. 3 and the droplet height H as $(\partial U/\partial z)_c \approx U_H/H$. The corresponding evolution for $(\partial U/\partial z)_c$,

reported in Fig. 8 (c), appears very similar to those obtained for laminar boundary layers and still follows a linear evolution with the theoretical scaling law (Eq. 1), again with different lines dependant on the air velocity U_∞ far from the substrate. Another approach to predict the onset of sliding resides on a critical Weber number obtained through a force balance approach [10, 12–16, 18–20]. At the onset of sliding, the aerodynamic force overcomes the capillary force. Thus, assuming that the droplet shape remains close to a spherical cap with a width W and a height H , this force balance reads:

$$\frac{1}{2}\rho_a U_m^2 C_d \pi H W \simeq \sigma W (\cos(\theta_r) - \cos(\theta_a)) \quad (2)$$

where ρ_a is the air density, C_d is the droplet drag coefficient, and U_m is the mean air velocity impacting the droplet. For experiments in laminar boundary layer, the mean velocity is given by $U_m = \frac{U_H}{2}$ as the portion of the boundary layer profile impacting the droplet is linear (i.e. $\frac{H}{\delta} < 5$). For experiments in turbulent boundary layer, the previous comparison with the theoretical scaling law (Eq. 1) suggests that taking $U_m = \frac{U_H}{2}$ is acceptable even if the portion of the boundary layer profile impacting the droplet is no longer linear. Thus, the force balance (Eq. 2) can be converted into a critical Weber number as

$$We_c = \frac{\rho_a U_H^2 H}{\sigma} \simeq \frac{8(\cos(\theta_r) - \cos(\theta_a))}{\pi C_d} \quad (3)$$

It is noticeable that the drag coefficient in Eq. 3 depends on the Reynolds number $Re_H = \frac{2U_H H}{\nu_a}$, that varies between 50 and 450 in our experiments. The drag coefficient for an hemispherical bubble set fixed on wall in a linear shear flow has been proposed by Legendre *et al.* [24]. The proposed relation connects the analytical solution under Stokes flow condition ($Re_H \ll 1$) and the asymptotic limit at large Reynolds number ($Re_H \gg 1$) obtained using direct numerical simulation leading to $C_d = \frac{16}{Re_H} + C_d^\infty = \frac{16}{Re_H} + 0.137$. The extension of the Stokes solution in the limit $Re_H \ll 1$ from the bubble to the solid hemisphere is straightforward and gives $C_d = 24/Re_H$. The limit at large Reynolds number is reported in Nardone *et al.* [25] and in Saal *et al.* [26] where $C_d^\infty = 0.40$, so we propose the following relation to provide the description of the drag coefficient of a solid hemisphere in a linear shear flow as:

$$C_d = \frac{24}{Re_H} + 0.40 \quad (4)$$

Figure 9 presents the measured critical Weber number with the prediction (Eq. 3 combined with Eq. 4) for a water droplet in a laminar and turbulent boundary layer (open and close symbols respectively) and for a glycerin droplet in a laminar boundary layer.

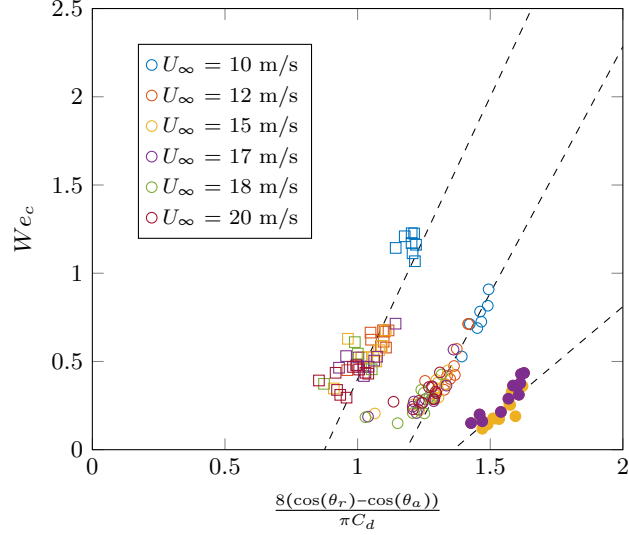


FIG. 9: Evolution of the critical Weber number, We_c for water and glycerol, as a function of $8[\cos(\theta_r) - \cos(\theta_a)]/(\pi C_d)$. (\circ), Water droplets; (\square), Glycerol droplets. Droplets immersed in a laminar boundary layer are represented in open symbols and in solid symbols for a turbulent boundary layer.

As one can see, linear trends independent of the airflow velocity U_∞ are now observed but the slopes appear to be dependent on the fluid and on the type of boundary layer (which is not surprising in regards of the "crude" approximation made for the mean air velocity for the turbulent boundary layer). The observed dependence on the fluid, suggests that the droplet viscosity (other physical properties being similar) has also an effect on the onset of sliding. This effect may be linked to the development of a recirculation inside the droplet prior to its sliding. Such recirculation has been observed numerically [9] and an effect of the viscosity ratio on the onset of sliding has already been suggested [8, 9]. Indeed, the recirculation inside the droplet is induced by the airflow through the tangential viscous shear stress at the interface. The magnitude of the recirculation is then connected to the external air flow with the viscosity ratio μ_a/μ . To confront our prediction with the results of the literature, we select in Table I the experiments performed for water droplets in laminar boundary layer (for which it is possible to compute the air velocity at the top of the droplet U_H) and plot them together with our experiments with water droplet in laminar boundary layer in Fig. 10.

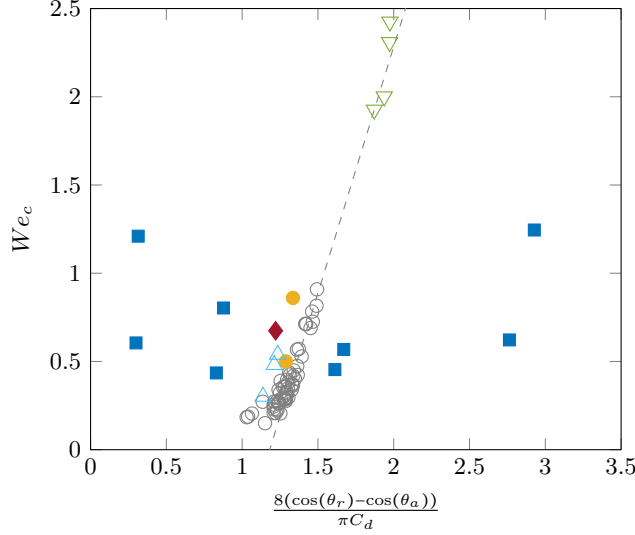


FIG. 10: The distribution of critical Weber numbers determined using the shear stress $(\partial U/\partial z)_c$ as defined in the text for both our data and the literature on water droplets in Laminar flow, function of $8[\cos(\theta_r) - \cos(\theta_a)]/[\pi C_d]$. (\circ), Water droplet - Our data; (\bullet), Milne and Amirfazli - 2009, (\blacksquare), Roisman *et al.* - 2015; (\blacklozenge), Hooshanginejad and Lee - 2017; (\blacktriangle), White and Schmucker - 2021; (\blacktriangledown), Zhang - 2021. The symbols represent different droplet sizes with respect to the boundary layer: open symbols for $H/\delta < 5$ and solid symbols for $H/\delta > 5$

As one can see, both our data and the ones from the literature appear to follow the same linear trend (except for the data of Roisman *et al.* [14]). This confirms that our prediction captures well the physics behind the onset of sliding. Note that the Reynolds number has a strong influence on the droplet onset of sliding due to the dependency of the drag coefficient with the Reynolds number for the system considered here.

C. Transition between shapes

After the onset of sliding, the droplet can adopt various shapes depending on experimental conditions (droplet volume and airflow velocity). The transition from oval to corner shape is difficult to characterize with only the side view as the wedge formation is only accessible from the bottom view. Nevertheless, as the droplet length strongly evolves during the transition from corner to rivulet shape, it may be possible to characterize the transition from oval to corner shape thanks to the evolution of the droplet length. Figure 11 presents

the length evolution with time for two different air velocities and for a water droplet of volume $V_d = 40 \mu\text{L}$ in dimensionless form ($\bar{L} = L/L_0$, L_0 being the initial droplet length, and $\bar{t} = t/t_f$, t_f being the time when the droplet reaches the end of the field of view). As one can see, when the droplet adopts an oval shape, its length varies by less than 12%, while corner shape and rivulet shape are characterized by a larger variation allowing to characterize the transition between oval and corner shape on the evolution of the length.

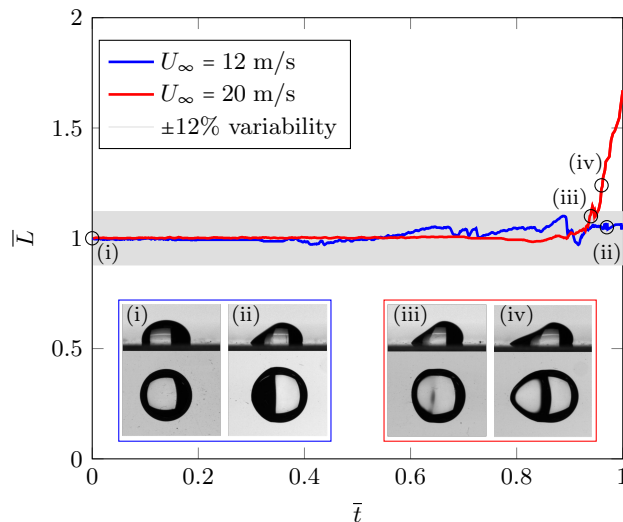


FIG. 11: Dimensionless Length \bar{L} of the droplet function of dimensionless time \bar{t} to show the condition of transition between oval and corner for two different velocities $U_\infty = 12$ and 20 m/s .

Figures 12 and 13 show respectively the evolution of the contact angles and the dimensionless length with the capillary number $Ca = \frac{\mu_d U_d}{\sigma}$ (μ_d being the droplet viscosity and U_d the droplet velocity). As one can see in Fig. 12 (a), the contact angles for water droplets only evolve at the beginning of sliding and rapidly reach constant values. Fig. 13 (a) shows that the droplet length clearly begins to evolve while the contact angles have reached their constant values. For glycerin droplet (see Fig. 12 (b) and Fig. 13 (b)), similar evolution can be observed even if the downstream contact angle appears to evolve until the droplet adopts a rivulet shape.

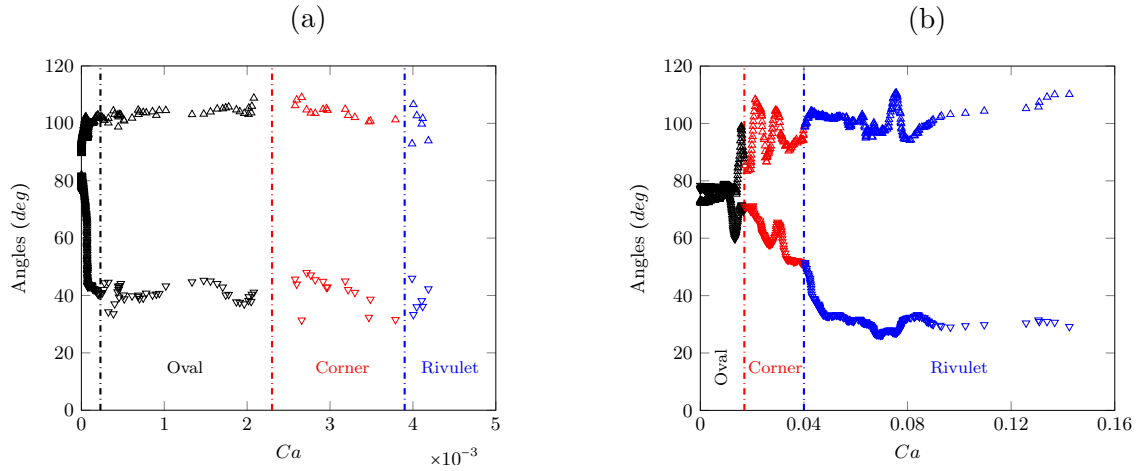


FIG. 12: Advancing and Receding contact angles function of the Capillary number. (a): water Droplet. (b): Glycerol Droplet. (Δ), Advancing contact angle θ_a ; (∇), Receding contact angle θ_r .

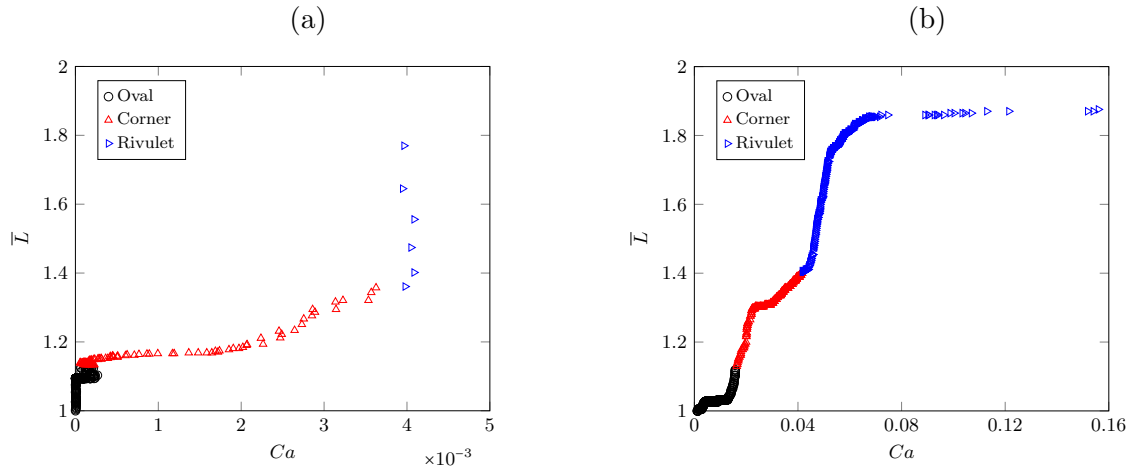


FIG. 13: Time evolution of the droplet's length as a function of Capillary number. (a): Water Droplet. (b): Glycerol Droplet.

It is interesting to notice that the contact angle evolution with the Capillary number differs from the expected Cox-Voinov evolution and that the droplet length evolution appears to be significant when the contact angles have reached almost constant values. Thus one can expect a strong coupling between the droplet shape and its velocity. To confirm these results, phase diagrams of droplet shape in terms of capillary and Bond ($Bo = \Delta\rho g L_0^2/\sigma$) numbers are presented in Fig. 14 for glycerin and water droplets.

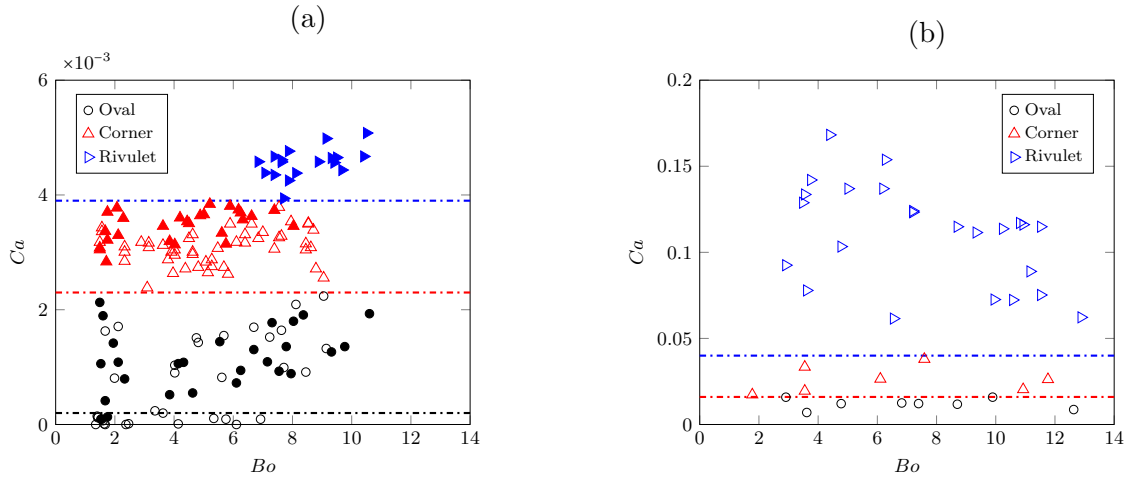


FIG. 14: Capillary number Ca function of Bond number Bo . Droplets immersed in laminar boundary layer are represented in open symbols and in solid symbols for turbulent boundary layer. (a): Water Droplet. (b): Glycerol Droplet.

These phase diagrams clearly show the link between the droplet shapes and the capillary number. It also appears that the rivulet shape only exists for a sufficiently large Bond number of order of 6.8 for water droplets and 3.2 for glycerin droplets. One can also remark that the capillary numbers for transition between shapes differ from water droplets to glycerin droplets. This confirms that the air-droplet viscosity ratio plays an important role in the transition between the shapes. A similar effect was observed for droplets sliding along an inclined wall [6].

IV. CONCLUSION

In this work, droplet sliding induced by an airflow on a horizontal surface has been studied experimentally. The onset of sliding is described thanks to a critical Weber number based on a force balance approach. This Weber number, based on the mean airflow velocity impacting the droplet, is dependent on the contact angle hysteresis, and the droplet drag coefficient itself depends on the Reynolds number. A relation for the dependence of the drag coefficient with the Reynolds number for an hemispherical droplet in a linear shear flow is proposed and used for the critical number prediction. This proposed Weber number appears to be in good agreement with our experiments and those from literature but appears to depend on

the droplet viscosity. This dependence upon the droplet viscosity appears as an interesting perspective but needs more experiments with other viscosities. The various shape of a sliding droplet (oval, corner, and rivulet) has been determined and their transitions appear to be directly linked to the capillary number. It is interesting to notice that the rivulet shape only appears for sufficiently large droplets.

-
- [1] J. J. Bikerman, “Sliding of drops from surfaces of different roughnesses,” *Journal of Colloid Science* **5**, 349–359 (1950).
 - [2] C. G. L. Furmidge, “Studies at phase interfaces. i. the sliding of liquid drops on solid surfaces and a theory for spray retention,” *Journal of Colloid Science* **17**, 309–324 (1962).
 - [3] E. B. Dussan and R. Chow, “On the ability of drops or bubbles to stick to non-horizontal surfaces of solids,” *Journal of Fluid Mechanics* **137**, 1–29 (1983).
 - [4] E. B. Dussan, “On the ability of drops or bubbles to stick to non-horizontal surfaces of solids. part 2. small drops or bubbles having contact angles of arbitrary size,” *Journal of Fluid Mechanics* **151**, 1–20 (1985).
 - [5] T. Podgorski, J. M. Flesselles, and L. Limat, “Corners, cusps, and pearls in running drops,” *Phys. Rev. Lett.* **87**, 036102 (2001).
 - [6] N. Le Grand, A. Daerr, and L. Limat, “Shape and motion of drops sliding down an inclined plane,” *Journal of Fluid Mechanics* **541**, 293–315 (2005).
 - [7] R. L. Inmaculada, E. Sotiris, K. Margaritis, Z. Xenophon, and D. K. Thodoris, “Effect of initial droplet shape on the tangential force required for spreading and sliding along a solid surface,” *Colloids and Surfaces A: Physicochemical and Engineering Aspects* **549**, 164–173 (2018).
 - [8] E. B. Dussan, “On the ability of drops to stick to surfaces of solids. part 3. the influences of the motion of the surrounding fluid on dislodging drops,” *Journal of Fluid Mechanics* **174**, 381–397 (1987).
 - [9] P. Dimitrakopoulos and J. Higdon, “Displacement of fluid droplets from solid surfaces in low-reynolds-number shear flows,” *Journal of Fluid Mechanics* **336**, 351–378 (1997).
 - [10] A. Milne and A. Amirfazli, “Drop shedding by shear flow for hydrophilic to superhydrophobic surfaces,” *Langmuir* **25**, 14155–14164 (2009).

- [11] J. Fan, M. C.T. Wilson, and N. Kapur, “Displacement of liquid droplets on a surface by a shearing air flow,” *Journal of Colloid and Interface Science* **356**, 286–292 (2011).
- [12] S. Moghtadernejad, M. Mohammadi, M. Jadidi, M. Tembely, and A. Dolatabadi, “Shear Driven Droplet Shedding on Surfaces with Various Wettabilities,” *SAE International Journal of Aerospace* **6** (2013), 10.4271/2013-01-2176.
- [13] S. C. Fu, W. T. Leung, and Christopher Y.H. Chao, “Detachment of droplets in a fully developed turbulent channel flow,” *Aerosol Science and Technology* **48**, 916–923 (2014).
- [14] I. V. Roisman, A. Criscione, C. Tropea, D. K. Mandal, and A. Amirfazli, “Dislodging a sessile drop by a high-reynolds-number shear flow at subfreezing temperatures,” *Physical Review E* **92**, 023007 (2015).
- [15] P. M. Seiler, M. Gloerfeld, I. V. Roisman, and C. Tropea, “Aerodynamically driven motion of a wall-bounded drop on a smooth solid substrate,” *Phys. Rev. Fluids* **4**, 024001 (2019).
- [16] B. Barwari, S. Burgmann, A. Bechtold, M. Rohde, and U. Janoske, “Experimental study of the onset of downstream motion of adhering droplets in turbulent shear flows,” *Experimental Thermal and Fluid Science* **109**, 109843 (2019).
- [17] B. Barwari, S. Burgmann, and U. Janoske, “Hydrodynamic Instabilities of Adhering Droplets Due to a Shear Flow in a Rectangular Channel,” *Chemie Ingenieur Technik* **91**, 991–1000 (2019).
- [18] L. Ma, Y. Liu, and H. Hu, “An experimental investigation on wind driven droplet moving on surfaces with different wettabilities,” *AIAA Scitech* (2019), 10.2514/6.2019-0632.
- [19] E. B. White and J. A. Schmucker, “Wind- and gravity-forced drop depinning,” *Phys. Rev. Fluids* **6**, 023601 (2021).
- [20] X. Zhang, *Interaction of water droplets residing on a solid surface with wall-bounded shear flows*, Ph.D. thesis, University of Waterloo (2021).
- [21] A. Hooshanginejad and S. Lee, “Dynamics of a partially wetting droplet under wind and gravity,” *Physical Review Fluids* **7**, 033601 (2022).
- [22] A. Hooshanginejad and S. Lee, “Droplet depinning in a wake,” *Phys. Rev. Fluids* **2**, 031601 (2017).
- [23] X. Zhang, B.A. Tuna, S. Yarusevych, and S. D. Peterson, “Flow development over isolated droplet-inspired shapes,” *International Journal of Heat and Fluid Flow* **88**, 108756 (2021).

- [24] D. Legendre, C. Colin, and T. Coquard, “Lift, drag and added mass of a hemispherical bubble sliding and growing on a wall in a viscous linear shear flow,” **366**, 2233–2248 (2008).
- [25] P. Nardone and K. Koll, “Velocity field and drag force measurements of a cube and a hemisphere mounted on an artificial bed surface roughness. e3s web conf 40: 05022,” (2018).
- [26] A. Saal, P. M. Seiler, D. Rettenmaier, M. Ade, I. V. Roisman, R. Berger, H. Butt, and C. Tropea, “Shuffling gait motion of an aerodynamically driven wall-bound drop,” *Physical Review Fluids* **5**, 094006 (2020).